Check for updates

JGR Solid Earth

RESEARCH ARTICLE
10.1029/2021JB022649

Special Section:
Machine learning for Solid Earth observation, modeling and understanding

Deep Learning for Efficient Microseismic Location Using Source Migration-Based Imaging

Qingshan Zhang[1], Wei Zhang[2,3], Xinming Wu[1], Jie Zhang[1], Wenhuan Kuang[3], and Xu Si[1]

[1]School of Earth and Space Sciences, University of Science and Technology of China, Hefei, China, [2]Shenzhen Key Laboratory of Deep Offshore Oil and Gas Exploration Technology, Southern University of Science and Technology, Shenzhen, China, [3]Department of Earth and Space Sciences, Southern University of Science and Technology, Shenzhen, China

Key Points:

- We apply deep learning to the microseismic location using source migration-based imaging and achieve better accuracy and efficiency
- We employ a 3D U-Net to solve the regression problem by focusing the symmetric pattern in diffraction stacking images
- We train the neural network by synthetic datasets, and it works well with input field data for detecting and locating events

Correspondence to:
W. Zhang and X. Wu,
zhangwei@sustech.edu.cn;
xinmwu@ustc.edu.cn

Citation:
Zhang, Q., Zhang, W., Wu, X., Zhang, J., Kuang, W., & Si, X. (2022). Deep learning for efficient microseismic location using source migration-based imaging. *Journal of Geophysical Research: Solid Earth*, *127*, e2021JB022649. https://doi.org/10.1029/2021JB022649

Received 21 JUN 2021
Accepted 19 FEB 2022

Author Contributions:
Data curation: Qingshan Zhang
Formal analysis: Wei Zhang
Investigation: Wei Zhang
Methodology: Qingshan Zhang, Wei Zhang, Xinming Wu, Jie Zhang
Resources: Wei Zhang
Software: Qingshan Zhang, Xu Si
Validation: Qingshan Zhang
Visualization: Qingshan Zhang
Writing – original draft: Qingshan Zhang, Wei Zhang, Jie Zhang
Writing – review & editing: Qingshan Zhang, Wei Zhang, Xinming Wu, Wenhuan Kuang

© 2022. American Geophysical Union. All Rights Reserved.

Abstract Migration-based location methods (e.g., time-reverse imaging based on wave equation, Kirchhoff summation, and diffraction stacking) can effectively locate events of low signal-to-noise ratios by stacking waveforms from many receivers. The methods have been widely applied for surface microseismic monitoring. However, these methods may not produce accurate results if there are polarity reversals in the surface records for a double-couple or even a general moment tensor event. Various imaging conditions have been developed to solve the non-focus image problem for a non-explosive source. Here, we propose a deep convolutional neural network to predict a better-focused image from a regular migration image that contains a quasi-symmetric pattern in both space and time. To train the network, we first simulate a large number of surface records from sources with various locations and mechanisms. We then compute diffraction stacking images from the records and take the images as the input to the network. We define the corresponding training labels as images (with the same size as the input) with Gaussian distributions centered at the true sources. This network, trained by only synthetic datasets, works well in field data to detect source locations from images for unknown events. Both synthetic tests and field data applications demonstrate that the proposed method can effectively improve diffraction stacking images for efficient microseismic location.

Plain Language Summary A new source location method is proposed for accurately and efficiently locating microearthquakes. Deep learning is introduced to compute better-focused source images from source migration imaging. We take the diffraction stacking image as the input of a neural network and train it using a Gaussian distribution centered on the true source using synthetic datasets. We apply the trained network to field data. The method shows good performance on noise suppression for weak events from field data.

1. Introduction

Seismic location is one of the most basic problems in seismology (Geiger, 1912; Kao & Shan, 2004; Richards et al., 2006). It is important for the research of seismicity activities, such as geological hazard monitoring (Zhang et al., 2020), safety monitoring in the mining industry (Li & Zhao, 2012), and induced seismicity monitoring in oil or gas exploitation (Li et al., 2011; Maxwell & Urbancic, 2001). Accurately locating the events is essential for better delineating the subsurface fault structures in both natural and induced earthquakes.

Many traditional methods have been developed to locate various types of sources. Firstly, the arrival-time-based location methods have been widely used to efficiently locate seismic events. This type of method is typically based on the traveltime inversion (Geiger, 1912), the master event (Ito, 1985), the double-difference (Waldhauser & Ellsworth, 2000), and reverse travel time imaging (Ge et al., 2019). However, these methods typically require arrival picking and inaccurate picking may decrease the location precision, especially for events with low signal-to-noise ratios (SNR). Secondly, the waveform-based location methods are proposed and they can effectively locate the weak events. Shelly et al. (2007) and Peng and Zhao (2009) have successfully applied the template-matching methods to detect and locate the non-volcanic tremor and aftershock. For locating microseismic events, Zhang and Zhang (2016) developed a microseismic search engine to estimate source location for downhole monitoring. The migration-based location methods, such as wave-equation-based time-reverse imaging (TRI, Artman et al., 2010; Kawakatsu & Montagner, 2008) and ray-theory-based diffraction stacking imaging (Duncan, 2005; Kao & Shan, 2004), have been widely used for the microseismic location as well. However, these methods suffer from huge calculation costs, especially for the surface array with a large number

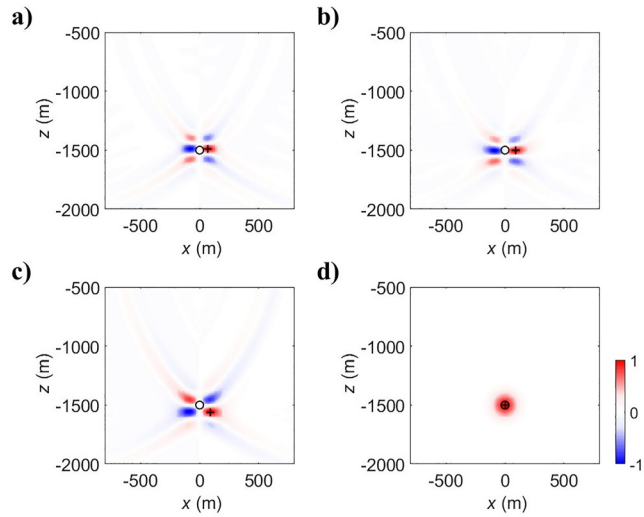

Figure 1. The quasi-symmetric pattern obtained at source origin time by (a) the TRI, (b) the Kirchhoff summation, and (c) the diffraction stacking. (d) Is the ideal source image whose maximum is located at the true source position indicated by the black circle. The black crosses indicate the maximum of the corresponding migration images.

of receivers. Recently, deep learning has been introduced to locate induced seismicity (Kriegerowski et al., 2019; Perol et al., 2018; Saad & Chen, 2020; Zhang et al., 2020).

Among the above methods, the migration-based location methods have the power of stacking a large number of waveforms and show great merits in enhancing the SNR of microseismic events, as a result, migration-based methods are widely adopted to locate the weak events whose first arrivals are difficult to pick. However, the hydraulic fractures usually contain many shear sources (Maxwell, 2014), resulting in polarity reversal during receivers at

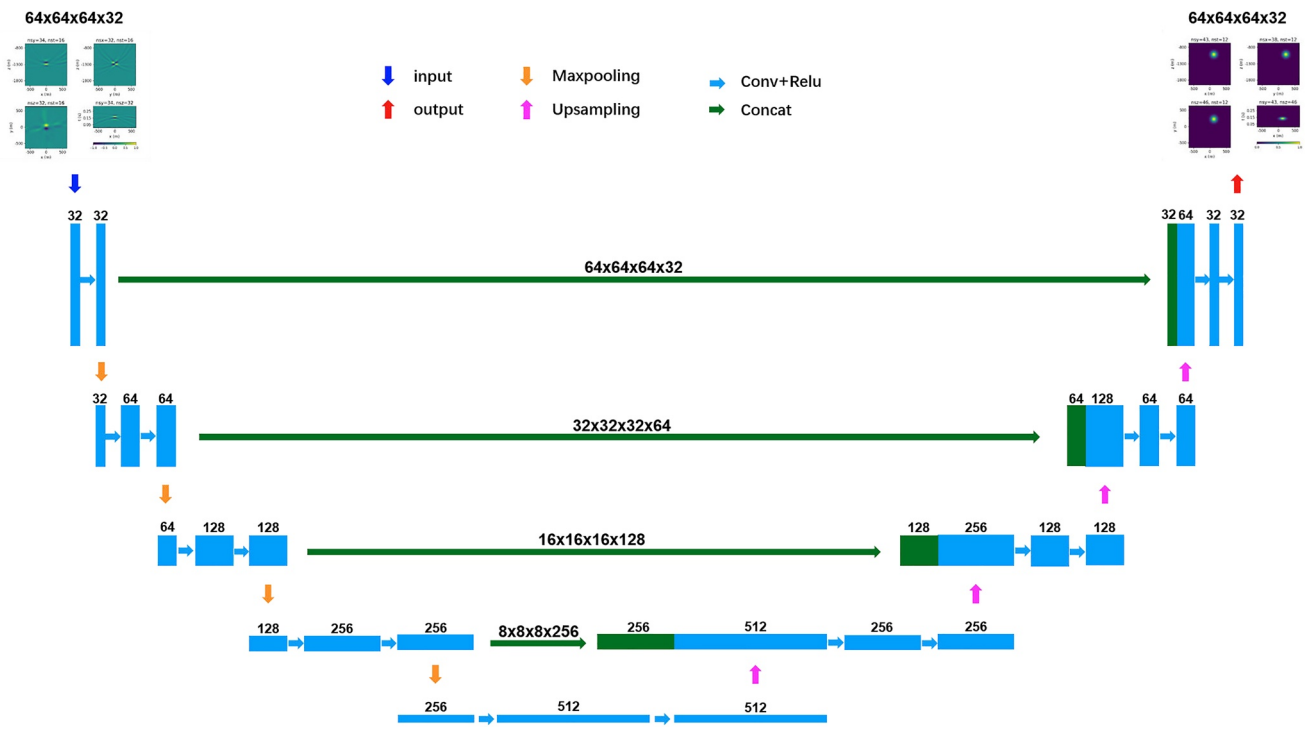

Figure 2. The architecture of the 3D U-Net. The 3D convolution operations are used for all convolution layers.

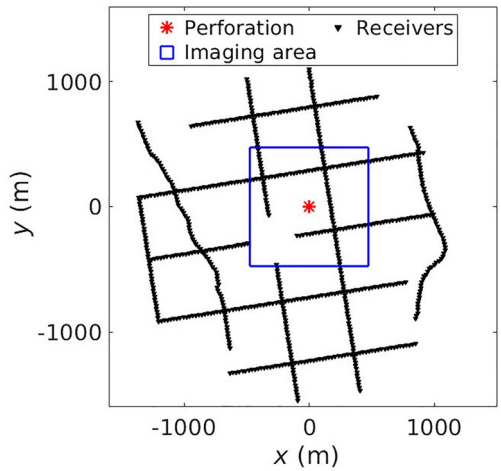

Figure 3. A real surface array for microseismic location during hydraulic fracturing.

different azimuths. Taking a pure shear strike-slip source with a symmetrically distributed surface array as an example, the migration image exhibits a quasi-symmetric distribution corresponding to the source radiation pattern. The center of this quasi-symmetric distribution indicates the true source in both the space and time domain and its imaging value is almost zeros. Thus, migration imaging cannot obtain the true source location by directly using the maximum imaging condition. To solve this problem, previous studies have developed many traditional techniques, which can be divided into two major categories: (a) correcting the polarity of the waveform before migration; (b) correcting the migration image by appropriate imaging conditions to focus the quasi-symmetric pattern onto its center. In the former case, the raw waveforms for migration can be replaced by their character functions to cancel the impact of polarity reversal. The character functions included absolute value (Kao et al., 2006; Kao & Shan, 2004), envelope (Kao & Shan, 2007), short time average to long time average ratio (STA/LTA; Grigoli et al., 2013, 2014), kurtosis (Langet et al., 2014), and coherency (Shi et al., 2018). The reversed polarity can also be corrected by source moment tensor inversion (Anikiev et al., 2014; Zhebel & Eisner, 2015), moment tensor imaging (Chambers et al., 2014), or focal mechanism search (Liang et al., 2016). The polarity corrections based on amplitude trend least-squares fitting (Xu et al., 2020) and convolutional neural network determination (Tian et al., 2020) were also applied to surface microseismic data. In the latter case, the imaging conditions for TRI mainly contained integral imaging, PS cross-correlation imaging (Artman et al., 2010), interferometric imaging (Li et al., 2014; Wang et al., 2013; Zhang & Zhang, 2022), the PS interferometric cross-correlation imaging (Zhou & Zhang, 2017; Zhou et al., 2022), energy imaging (Oren & Shragge, 2019; Rocha et al., 2019), and the geometric-mean imaging (Lyu & Nakata, 2020; Nakata & Beroza, 2015).

In addition to the unfocused problem of migration imaging, the traditional source detection based on a constant threshold often has false triggering due to the multi-extremums, especially for cases with outliers. In this study, we use deep learning to efficiently compute a better-focused source from migration image for microseismic location during hydraulic fracturing. The U-Net is firstly proposed for cell image segmentation in life science by Ronneberger et al. (2015) and has been widely used in many aspects of geophysics (Li et al., 2021; Wu et al., 2020; Yan & Wu, 2021). Due to the good performance of the U-Net on feature extraction, we use a 3D U-Net architecture modified from the widely used 2D U-Net to deal with the unfocused problem of migration imaging, and the network can also be regarded as a kind of imaging condition. Considering the calculation costs, we apply this imaging condition to diffraction stacking, even though it is suitable for both ray-based and wave-equation-based migration. We use synthetic datasets to train our network. The inputs of the network are the 4D diffraction stacking images (with the spatial-temporal quasi-symmetric patterns), and the labels are defined as the Gaussian distributions centered on true source locations. In this paper, we first explain the theory of migration imaging and the problem of polarity reversal. We then introduce the architecture of our 3D neural network designed for improving source migration images. We further describe the preparation of training data, training results, and error analysis of prediction. Finally, we apply the trained network to locate the microseismic events for field data.

Table 1
The Ranges of Source Parameters for 800 Random Sources

Parameters		Ranges
Source locations (m)	x	(−320, 320)
	y	(−320, 320)
	z	(−1,620, −980)
Source origin time (ms)	t	(10, 320)
Source mechanisms (˚)	strike	(0, 360)
	dip	(0, 90)
	rake	(0, 180)

2. Migration-Based Source Imaging

Among the migration-based method, TRI has the merits of precise recovery of the wavefield. TRI is a wave-equation-based migration method that uses the time-reversed records at surface stations as the boundary condition or source term to reconstruct wave propagation utilizing the wave equation, which can handle a complex velocity model. Kawakatsu and Montagner (2008) demonstrated that the time-reversal wavefield for the moment tensor source at $\boldsymbol{x}$ may be expressed as:

$$TR_{ij}(t) = E_{ij}^{n}(\boldsymbol{x}, t; \boldsymbol{r}, 0) * d_n(t_0 - t), \quad (1)$$

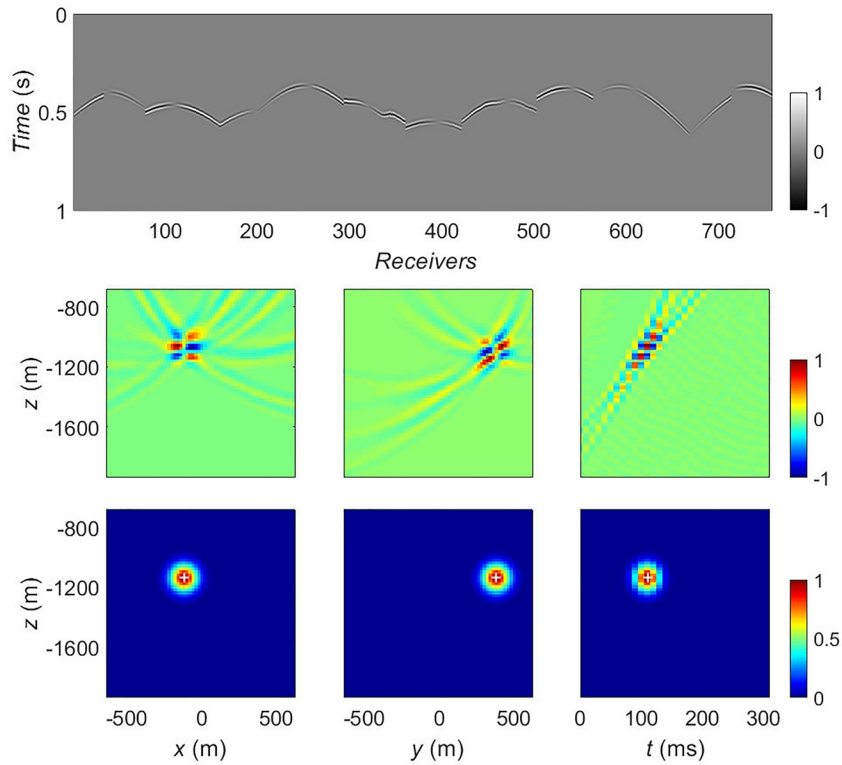

Figure 4. One of the noise-free samples. The upper panel shows the synthetic waveform. The middle panel indicates three slices of diffraction stacking image that is the input data of the network. The bottom panel indicates three slices of a Gaussian distribution centered on the source location (displayed by white crosses), that is the label of the network.

where $d_n(t)$ is nth component of observation waveform at a point $\boldsymbol{r}$; E_{ij}^n is the strain field due to a unit force directed to nth direction from $\boldsymbol{r}$ to $\boldsymbol{x}$; t_0 is an arbitrary reference time. In this case, the back-propagated wavefield will converge at the source location as the moment tensor and exhibit a quasi-symmetric distribution.

However, considering the large calculation costs of the time-reverse imaging method, we can use the ray-theory-based migration to improve the efficiency of the wavefield recovery. For example, the Kirchhoff summation can recover a similar quasi-symmetric pattern when the velocity is not too complex to have the multi-path effect or focusing and defocusing effects (Hung et al., 2001). The far-field P-wave Kirchhoff summation (Yilmaz, 2001) can be expressed as:

$$K(\boldsymbol{x}, t_0) = \frac{1}{4\pi} \sum_r \frac{\cos\theta}{\sqrt{vd}} \frac{\partial}{\partial t} u\left[\boldsymbol{r}, t_0 + tt(\boldsymbol{r}, \boldsymbol{x})\right], \tag{2}$$

where $1/\sqrt{vd}$ ($1/vd$ for 3D) represents spherical spreading, in which v and d are P-wave root-mean-square (RMS) velocity at receiver $\boldsymbol{r}$ and distance between imaging point $\boldsymbol{x}$ and receiver $\boldsymbol{r}$, respectively; $\cos\theta$ is obliquity factor and θ is the azimuth angle from imaging point $\boldsymbol{x}$ to receiver $\boldsymbol{r}$; the time derivative $\frac{\partial}{\partial t}$ indicates phase correction; u represents the displacement of receiver $\boldsymbol{r}$; tt is the P-wave traveltime.

The simplest migration method is diffraction stacking, which stacks the waveform only along the moveout curve. In terms of computational cost, diffraction stacking is more efficient than the wave equation and Kirchhoff summation. However, diffraction stacking omits the effects of the obliquity factor, spherical spreading, and phase correction in Equation 2; thus, the stacked wavefield is not the true wavefield. In this work, we apply directly stacking the records by using the following diffraction stacking equation:

$$S(\boldsymbol{x}, t_0) = \sum_r u\left[\boldsymbol{r},\ t_0 + tt(\boldsymbol{r}, \boldsymbol{x})\right]. \tag{3}$$

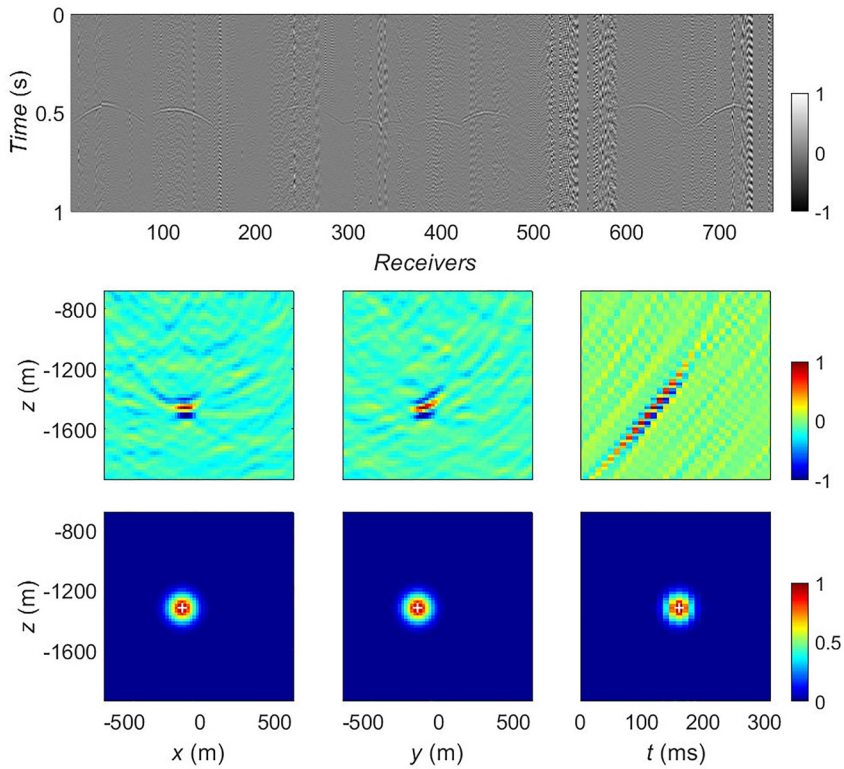

Figure 5. One of the noisy samples. The upper panel shows the synthetic waveform. The middle panel indicates three slices of diffraction stacking image that is the input data of the network. The bottom panel indicates three slices of a Gaussian distribution centered on the source location (displayed by white crosses), that is the label of the network.

We use a simple test to visually demonstrate the problem of polarity reversal for a 2D situation. A dip-slip source is deployed in a homogeneous medium and symmetric receivers are distributed on the surface. Figure 1a shows the result of TRI at origin time, and it exhibits some spatially quasi-symmetric features related to the source radiation pattern. Figure 1b shows the result of the Kirchhoff summation which has a similar quasi-symmetric distribution as TRI. The result of diffraction stacking is shown in Figure 1c which also exhibits a quasi-symmetric pattern although it has some differences from that of TRI and Kirchhoff summation. The true location is not located at the maximum of this migration image. In contrast, the image value is almost zero. Thus, we have to suppress the multi-extremum and correct this quasi-symmetric pattern to focus energy onto its center indicating the true source location as shown in Figure 1d.

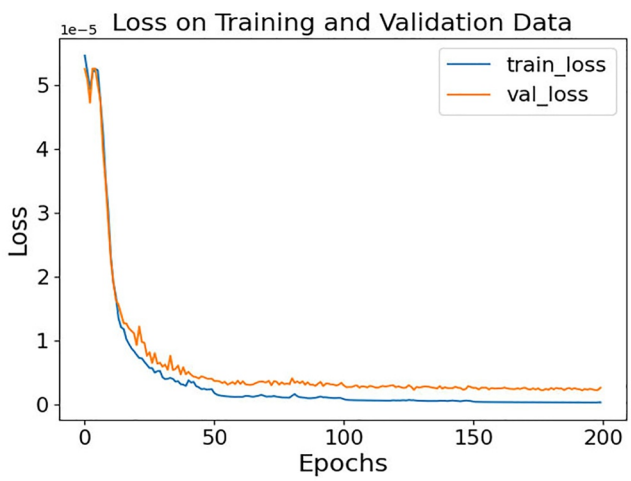

Figure 6. Loss curve of training and validation.

3. Deep Learning for Improving the Source Image

We propose a deep learning method to compute an improved focused source image (Figure 1d) from a regular diffraction stacking image (Figure 1c). We solve this regression problem by using a 3D U-Net architecture which is modified from the widely used 2D U-Net (Ronneberger et al., 2015).

3.1. Network Architecture

As shown in Figure 2, the 4D diffraction stacking image is taken as the input of the network. The size of input data is 64*64*64*32 which indicates the solution space of source parameters (x, y, z, t). Due to the convolution layers in our network being 3D convolution, we take the time dimension as the channel dimension in our network. After every two layers of 3D convolution, four down-sampling pooling layers are used to achieve the profile features.

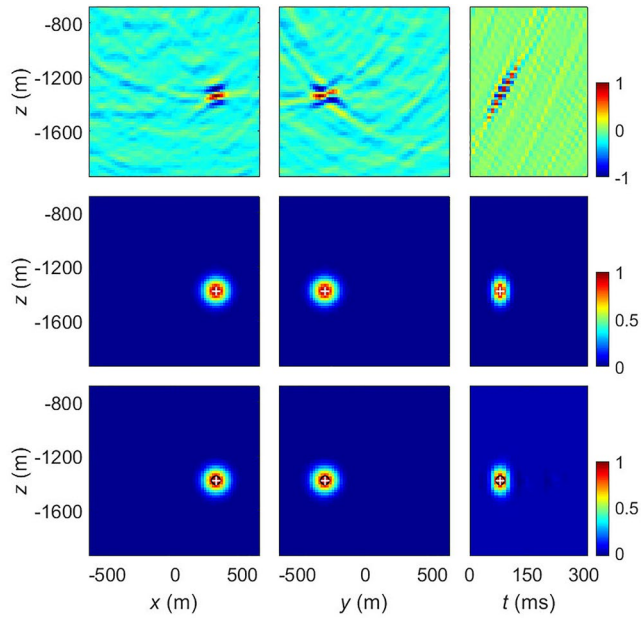

Figure 7. One of the noisy samples in validation datasets. The upper panel shows three slices of diffraction stacking image that is the input data of the network. The middle panel indicates three slices of a Gaussian distribution centered on the source location that is the label of the network. The bottom panel shows three slices of the prediction. The white crosses show the maximum of the label and indicate the true source location. The black circles show the maximum of prediction and indicate the source location predicted by the trained network.

Then, we obtain the output by four up-sampling layers and the following two layers of 3D convolution to achieve the same size as the input. The horizontal skip connections ensure that the output layers can obtain both profile and detail features from the input layers. The training label is defined as a Gaussian distribution centered on the true source location. Based on the recognition by U-Net, we transform the problem of pattern correction into a regression problem.

3.2. Data Preparation and Training

We adopt a real surface array for microseismic monitoring during hydraulic fracturing for coal-bed methane in China to simulate the synthetic waveform and produce images for training. 10 lines of receivers (black inverted triangles in Figure 3) are deployed to record microseismic signals during hydraulic fracturing. The array consists of 758 vertical component geophones with an average interval of approximately 25 m and the total spread is about 2,500 m. Our study is performed within a cube centered on the perforation (red star in Figure 3) with a 20 m spacing. The blue box in Figure 3 shows the horizontal projection of this cube with the range of 1,280 m in both horizontal and depth.

Since the microseismic events recorded by the surface array are dominated by shear failure, we just consider the double-couple sources in our training process. Eight hundred sources with random locations and source mechanisms are used to generate the datasets of input (stacking image) and label (Gaussian-shaped image). The ranges of locations and mechanisms for these random sources are shown in Table 1. The forward waveforms are computed using the elastic wave finite-difference code developed by Zhang and Chen (2006) and Zhang et al. (2012). Figure 4 shows one of the noise-free samples with the source location of (x, y, z, t) = (−120 m, 380 m, −1,140 m, 110 ms) and the source mechanism of (strike, dip, rake) = (0, 90, 0).

To train the network that can be applied to the real noisy data, we add different realistic noise waveforms to half samples (400 samples) of the training datasets and validation datasets. We assume the waveforms of the real data before any events recorded by the surface array in Figure 3 to be the realistic noise waveforms. We then take 1,000 ms noise waveforms each time to add to the synthetic waveforms of each sample. The starting times of the noise waveforms are different with 1 ms separation each time. The amplitudes of the noise waveform are scaled to

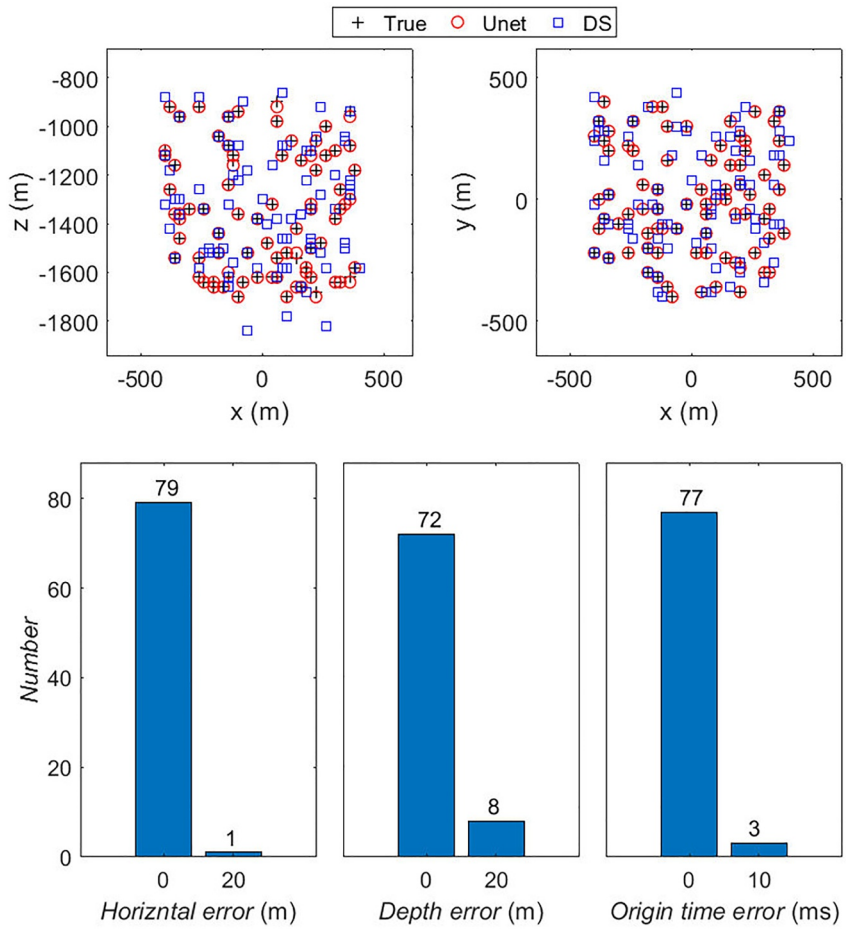

Figure 8. Location results of 80 events from validation dataset. The upper panel shows a comparison between true source locations (black crosses), predicted locations by using the trained network (red circles), and diffraction stacking (DS) locations (blue boxes); The bottom panel shows a statistic of location errors from network prediction. The numbers above the histograms indicate the number of samples corresponding to the errors.

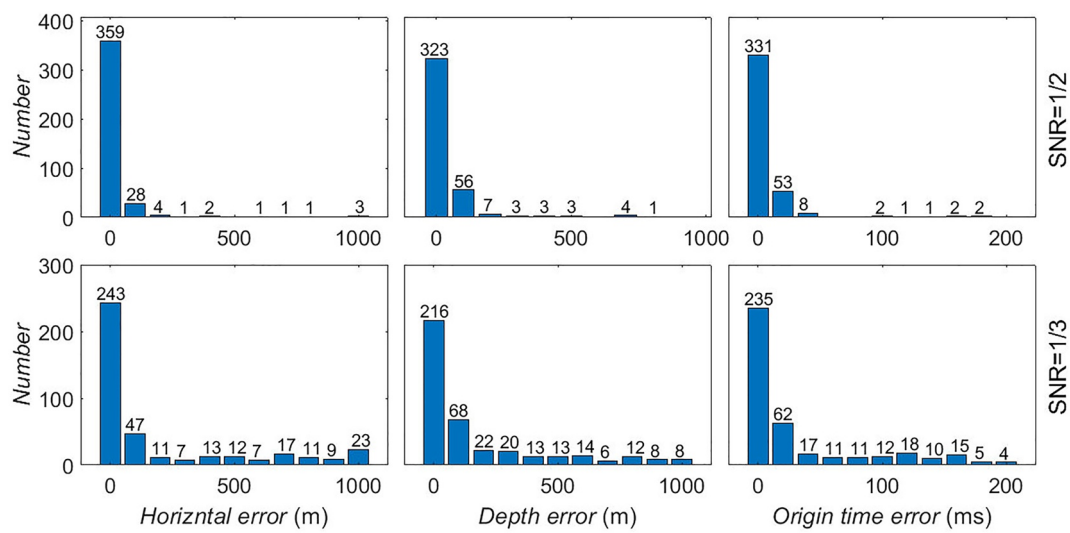

Figure 9. The statistics of prediction for noisy synthetic datasets with SNR are 1/2 (The upper panel) or 1/3 (the bottom panel).

Table 2
The Probability Distribution for Predicted Errors

Prediction errors		Probability (%) SNR = 1/2	SNR = 1/3
Horizontal	≤100 m	95.5	69.25
	≤200 m	96.75	74.5
Depth	≤100 m	93.75	68
	≤200 m	96.5	74.25
Origin time	≤20 ms	94	69.75
	≤40 ms	97.25	76.5

satisfy a pre-defined SNR level, which is defined as the ratio of the maximum absolute amplitude of synthetic waveforms of all the traces to that of all the noise waveforms. In this work, we use the SNR of 1 in the training process. Figure 5 shows one of the noisy samples with the source location of (x, y, z, t) = (−120 m, −140 m, −1,320 m, 160 ms) and the source mechanism of (strike, dip, rake) = (110, 73, 149).

For all 800 samples, we take both 360 noise-free and noisy samples as training datasets and both 40 noise-free and noisy samples as validation datasets. The designed network contains 23, 560, 096 training parameters. The loss function of mean square error (MSE) and dynamic learning rate are employed. The initial learning rate is 0.0004, and it is halved every 20 epochs. The batch size is set as nine. As shown in Figure 6, the loss of training and validation has converged with 200 epochs of training.

4. Example Application

After the training, we test the network on the validation datasets to verify the effectiveness of the trained network. Then we do some tests on an extra dataset with lower SNR to demonstrate the performance of the network on noise suppression.

4.1. Test on the Validation Dataset

To verify the performance of the trained network on validation datasets, Figure 7 shows a noisy validation dataset, in which the prediction (bottom row) of the input stacking image (top row) is almost the same as the label (middle row).

Figure 8 shows the location results of 80 events from the validation dataset. The top panel exhibits the comparison between the true source locations, the predicted locations by using the trained network, and the diffraction

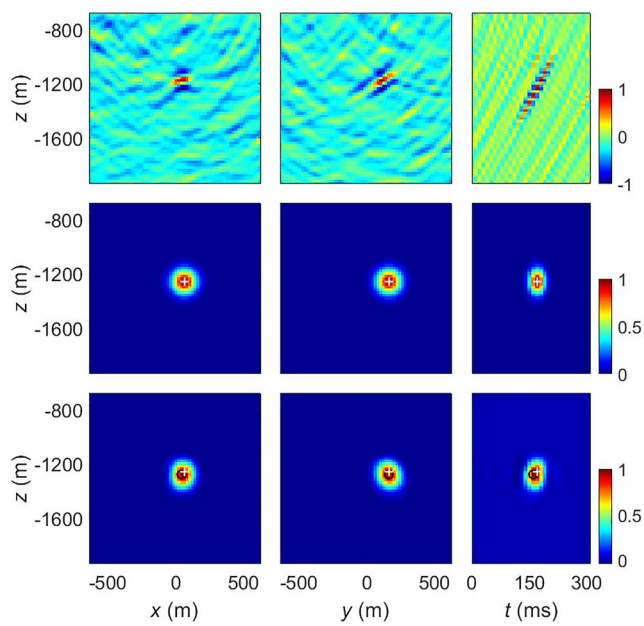

Figure 10. One of the noisy samples in test datasets with SNR of 1/2. The upper panel shows three slices of diffraction stacking image that is the input data of the network. The middle panel indicates three slices of a Gaussian distribution centered on the source location that is the label of the network. The bottom panel shows three slices of the prediction. The white crosses show the maximum of the label and indicate the true source location. The black circles show the maximum of prediction and indicate the source location predicted by the trained network.

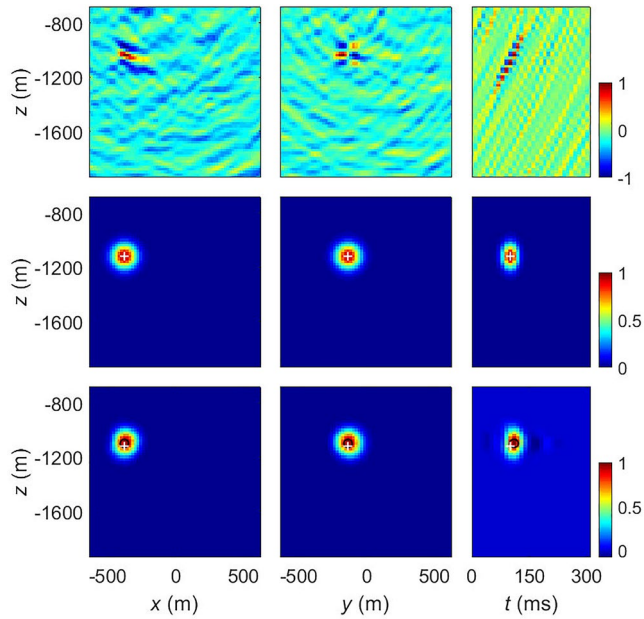

Figure 11. One of the noisy samples in test datasets with SNR of 1/3. The upper panel shows three slices of diffraction stacking image that is the input data of the network. The middle panel indicates three slices of a Gaussian distribution centered on the source location that is the label of the network. The bottom panel shows three slices of the prediction. The white crosses show the maximum of the label and indicate the true source location. The black circles show the maximum of prediction and indicate the source location predicted by the trained network.

stacking locations. Many diffraction stacking locations have estimation errors due to the maximal values of symmetric patterns are not located at true source positions (centers of quasi-symmetric patterns). The predicted locations have better consistency with true locations than diffraction stacking locations. The statistic location errors (including errors in horizontal, depth, and origin time) for network predictions, shown as the bottom panel in Figure 8, indicate that just a few predictions have errors of only one search grid (20 m in space and 10 ms in time). Besides, samples with horizontal prediction error are fewer than those with depth or origin time error. It means that the predictions for this trained network are more accurate in horizontal. This is consistent with the traditional location method due to the less constraint in the depth for surface microseismic records.

4.2. Test on Low SNR Dataset

We use the trained network to predict the noisy datasets with SNR of 1/2 and 1/3. To illustrate the effect of the prediction for this trained network, we count the location errors of the prediction for 400 synthetic samples with SNR of 1/2 and another 400 samples with SNR of 1/3. As shown in Figure 9, we count the number of errors in horizontal, depth, and origin time for these two datasets. Only a few predictions of datasets with SNR of 1/2 show large errors while the predictions of datasets with SNR of 1/3 are worse. Table 2 shows the probabilities associated with the prediction.

As shown in Figures 10 and 11, the input stacking images have stronger perturbations from noisy waveforms, and there are some obvious differences between prediction and label. Although the prediction fails to obtain the true source location, it is also concentrated around the source.

4.3. Velocity Perturbation

The velocity model is often poorly known in practical applications. The inaccurate velocity model will lead to the incorrect location for migration-based location methods. To check the sensitivity of the proposed method against velocity model perturbation, we apply some inaccurate velocity models to generate network inputs for

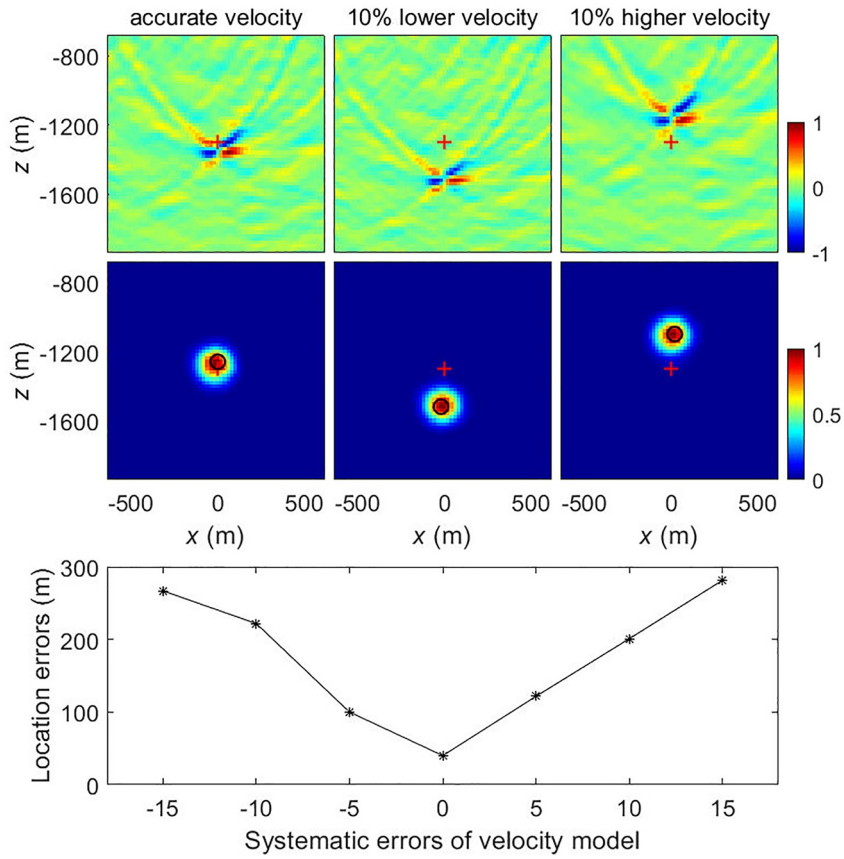

Figure 12. Network inputs (the top row) and predictions (the middle row) in x-z slices for accurate, 10% lower, and 10% higher velocity models. Red crosses and black circles indicate true source position and located source position, respectively. The bottom row shows location errors when the velocity models are accurate or have perturbations of ±5%, ±10%, and ±15%. The waveform of this sample has an SNR of 1.

a noisy sample with an SNR of 1. The top row of Figure 12 shows the diffraction stacking images in the x-z slice for accurate, 10% lower, and 10% higher velocity models. We can see that the diffraction stacking images produce quasi-symmetric patterns at the wrong locations due to the error of the velocity models, which can be expected as the absolute location of the events depends on the accuracy of the velocity model. Even though the shapes of the quasi-symmetric patterns at the wrong location vary a little bit for different velocity errors, the proposed method still can predict focused source images (the middle panel of Figure 12) using the trained network. The bottom row of Figure 12 shows location errors when velocity models are accurate or have ±5%, ±10%, and ±15% perturbations. This test demonstrates that we can obtain a focus source image by the trained network as long as the diffraction stacking image has a quasi-symmetric pattern.

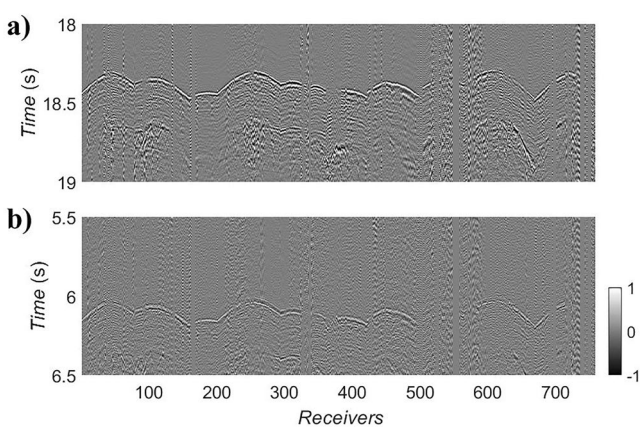

Figure 13. The normalized waveform of an event with higher SNR (a) and an event with lower SNR (b) in field data.

5. Field Data Application

In this section, we apply the network trained by synthetic datasets to field data. The field data are recorded by a surface array (Figure 2) during the hydraulic fracturing of coalbed methane in North China. The field data preprocessing includes (a) removing the mean values for each channel; (b) band-pass filtering between 5 and 70 Hz to eliminate high-frequency noise and low-frequency trends; (c) normalization for each trace to cancel the outliers; (d) statics correction.

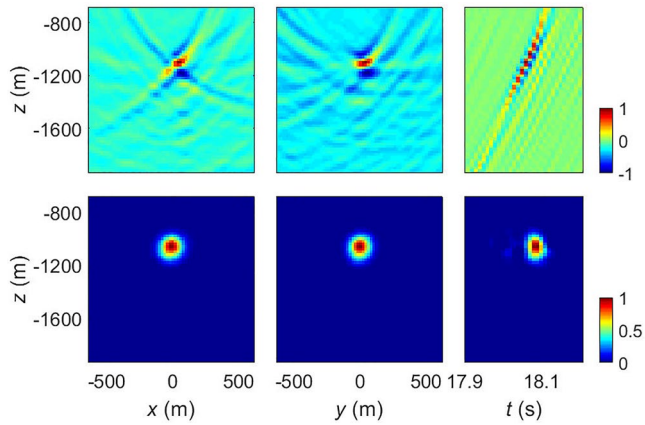

Figure 14. The upper panel shows three slices of diffraction stacking image of the event shown in Figure 13a which is the input data of the network. The bottom panel shows three slices of the prediction.

Due to the lack of a useable layer velocity model in the target area, an equivalent RMS velocity calibrated by the first visible event is used to generate input datasets for the trained network by diffraction stacking. We choose the same cube as in the synthetic to perform the field data location.

5.1. Individual Event

Firstly, two single events are used to exhibit the location performance of the trained network for field data. Figure 13 shows the normalized waveforms of an event with higher SNR at approximately 18.5 s and an event with lower SNR at approximately 6 s, respectively.

In Figure 14, the upper panel shows the input of the network, i.e., the diffraction stacking image of the event shown in Figure 13a. The bottom panel is the prediction of the trained network which shows a better-focused source image, especially on the time axis.

As same with Figures 14 and 15 shows the diffraction stacking and prediction of the trained network for the event shown in Figure 13b. The diffraction stacking image for this event has more perturbation. Even though this event is much weaker than the above strong event from the waveforms shown in Figure 13a, the stacking pattern is obvious as well. This is due to the great performance of noise suppression from diffraction stacking. The prediction of this weak event also shows a better-focused source image.

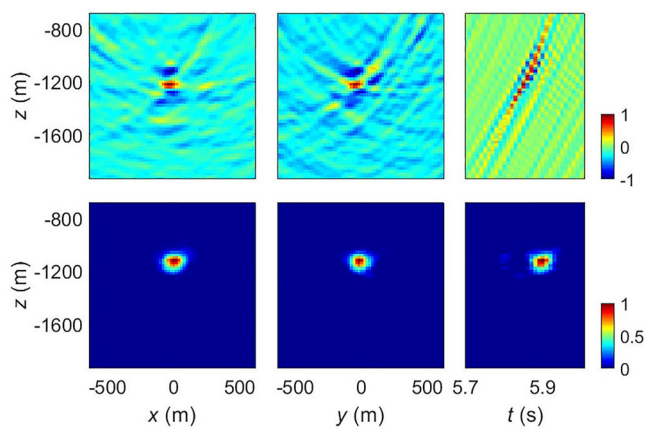

Figure 15. The upper panel shows three slices of diffraction stacking image of the event shown in Figure 13b which is the input data of the network. The bottom panel shows three slices of the prediction.

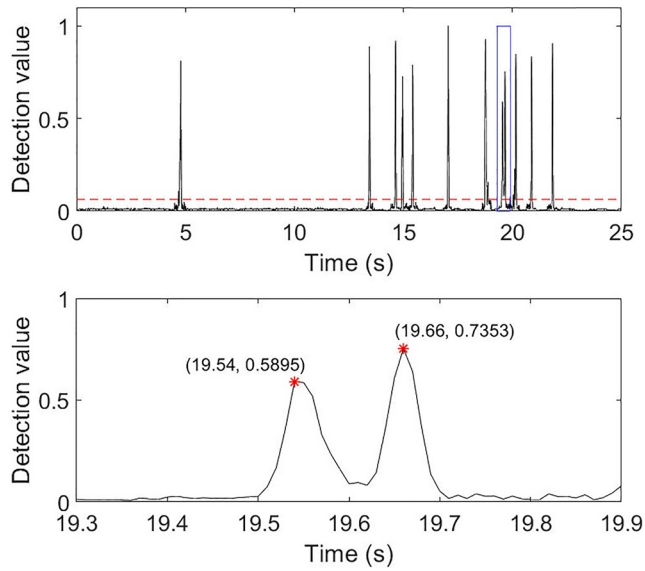

Figure 16. The upper panel is the detection curve of continuous surface records, in which the red dash line indicates the threshold of detection. The bottom panel shows the detail for the blue box in the upper panel. The red stars mark two close events.

5.2. Continuous Seismic Records

We further apply the trained network to 25 s continuous surface records. The records have been pre-processed by filtering and static correction. We split the time axis of the diffraction stacking image into a series of 320 ms segments with an interval of 10 ms. And there is a 160 ms overlap between two consecutive segments to avoid the arrival from one event being divided. Meanwhile, the space of the diffraction stacking image is constrained in a 64*64*64 cube around the perforation to ensure that the size of the diffraction stacking image is satisfied for the input of the trained network.

The upper panel of Figure 16 shows the detection result of the continuous records, in which the red dash line indicates the detection threshold. Generally, the threshold for microseismic detection is set as three times of background value (Trojanowski & Eisner, 2017). Here, we define the threshold as six times of background (the average of detection value from the first 4 s) value because the triggers of events are obvious.

We take two close events (shown as red stars in the bottom panel of Figure 16) as examples to assess the location results for network prediction. Figure 17 and Figure 18 show the location result for the event at 19.54 and 19.66 s,

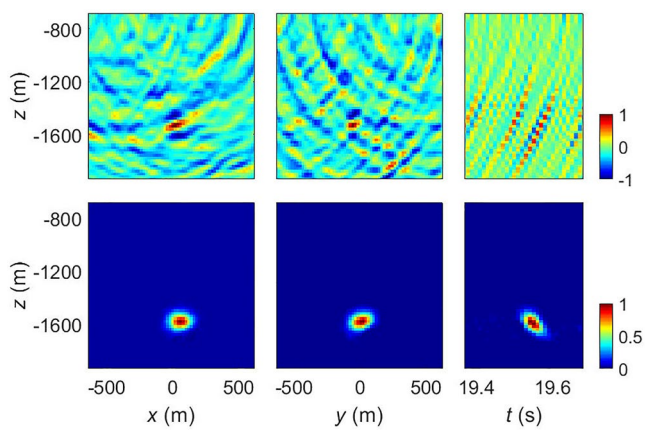

Figure 17. The input (the diffraction stacking image shown as upper panels) and the prediction of the network for the event at 19.54 s showed in Figure 16.

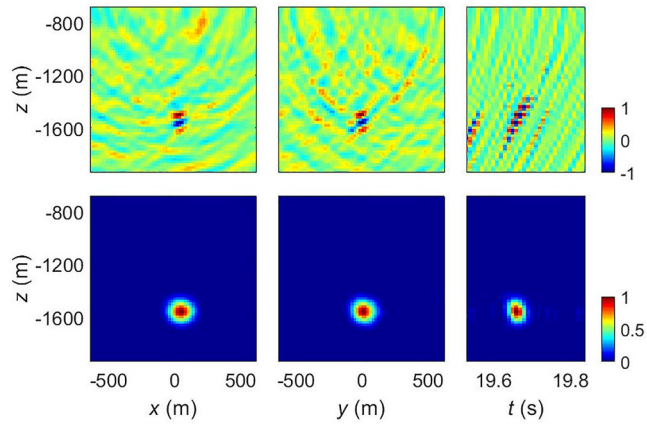

Figure 18. The input (the diffraction stacking image shown as upper panels) and the prediction of the network for the event at 19.66 s showed in Figure 16.

respectively. The upper panels are the diffraction stacking images for inputs of the network. And the bottom panels are the predictions of the network. The diffraction stacking images for these two events exhibit quasi-symmetric patterns with low SNR, especially for the event at 19.54 s. However, the trained network almost perfectly focuses symmetric patterns without any artifacts. It demonstrates that our proposed imaging condition based on deep learning can recognize the source from the migration image with very low SNR.

To verify the reliability of these two events detected by our trained network, we show the corresponding waveforms in Figure 19 and overlap the P wave arrivals computed by located events on the waveforms. The visible events at the marked P arrivals demonstrate that the detection and location for these two events are reliable. Even though the SNRs of these close two events are much lower than that of two single events shown in Figure 13, there are no significant differences in the effect of the predictions for these events. Unfortunately, we can see another visible event (shown as the yellow arrows in Figure 19) that is missed by our location procedure. This may be due to the very low SNR of the diffraction stacking image of this event. And, it also means that our trained network can be further improved to detect and locate more events with much lower SNR.

Finally, we apply the trained network on 30 min of field data and obtain 598 events with the same threshold in Figure 16. Figure 20 shows all detected events and the locations in horizontal and vertical cross-sections.

6. Discussion

Deep learning has not been widely applied for microseismic event locations in the seismic industry, because the training dataset (synthetic or real waveforms) depends on a correct velocity structure and observation system. Therefore, there is no universal training dataset for microseismic locations in any area. In this study, we introduce deep learning to predict locations from source migration images instead of from waveforms, thus separating

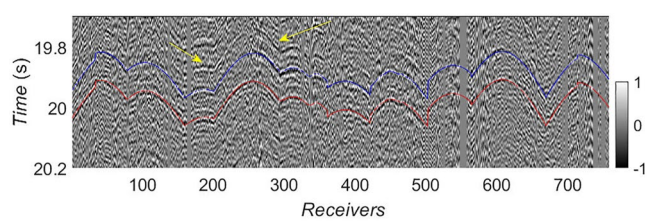

Figure 19. The waveform with two close events (shown in the bottom panel of Figure 16). The blue and red lines indicate the events shown in Figures 17 and 18, respectively. The yellow arrows show a visible event that was not detected by our location procedure.

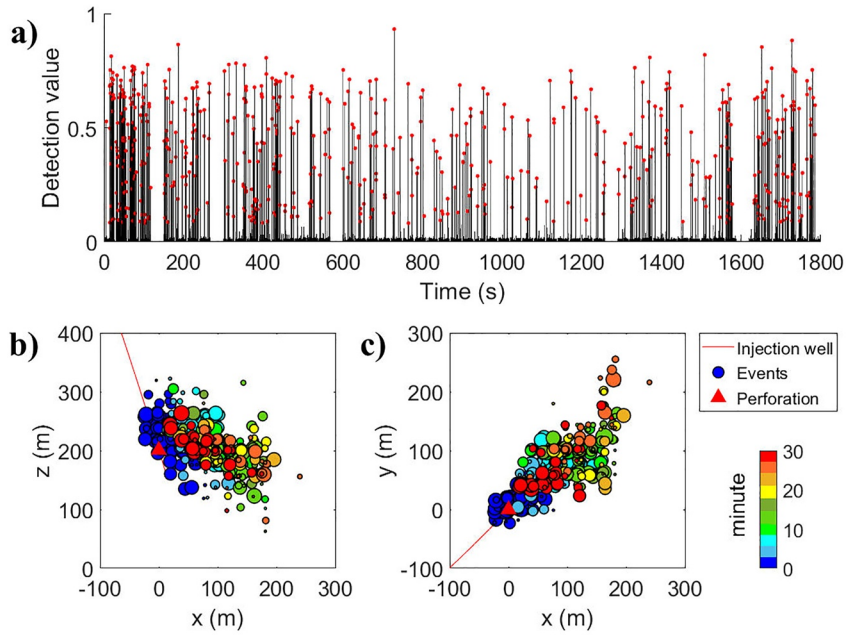

Figure 20. The detected events within 30 min of field data. (a) Shows the detection values for all data segments. Red dots indicate the detected events with the detection values larger than the given threshold. (b) and (c) show the location of events in the horizontal and vertical cross-sections. The colors and sizes of dots indicate source origin times and the detection values respectively.

the dependence of the velocity model from the deep learning step. We also note that the diffraction stacking method for the migration part is not-so-much sensitive to velocity models. Thus the whole training and prediction processes in our procedure are less dependent on different velocity models and geometries from different areas. We take two common geometries as examples to illustrate this point. Figures 21a and 21b show the sparse and the star-like surface array, respectively. The sparse array contains 50 receivers extracted from field geometry shown in Figure 3, and the star-like array contains 120 receivers, which are distributed on 8 arms with an interval of 100 m. We deploy a dip-slip source with mechanism of (strike, dip, rake) = (0, 90, 90) at the position of (x, y, z, t) = (0 m, 0 m, −1,300 m, 150 ms). Figures 21c and 21d shows the synthetic waveforms with a homogeneous velocity model (P wave velocity is 4,800 m/s). Due to the given source mechanism, the waveform shown in Figure 21d has zero amplitude on two arms (receivers 31–45 and receivers 91–105).

We apply the trained network to these two test samples with different geometries. Figures 22 and 23 show the inputs, labels, and predictions for sparse array and star-like array, respectively. Even though the predicted locations have slight errors, the trained network still has a good performance on the recognition and location for these two diffraction stacking images.

Even though we use a dense array from the real case for synthetic training and field data prediction, the sparse array shown in Figure 21a is also a common geometry for microseismic monitoring during hydraulic fracturing. We extract the real noise for the same receivers in this sparse array and add the noise to the synthetic waveform. The noise maximal equals the signal maximal. Figure 24 shows the input (diffraction stacking image), label, and prediction for this noisy sample. With the impact of noise, the diffraction stacking image is much noisier, but the prediction from the trained network still achieves a well-focused source image.

Theoretically, the network trained by one area can be directly applied to another area with different geometry and velocity model, even though an incorrect velocity model may lead to inaccurate locations. But in practice, it will be better to predict the source location by training the network again with the same geometry as the prediction data, the more accurate velocity model, and the real noise.

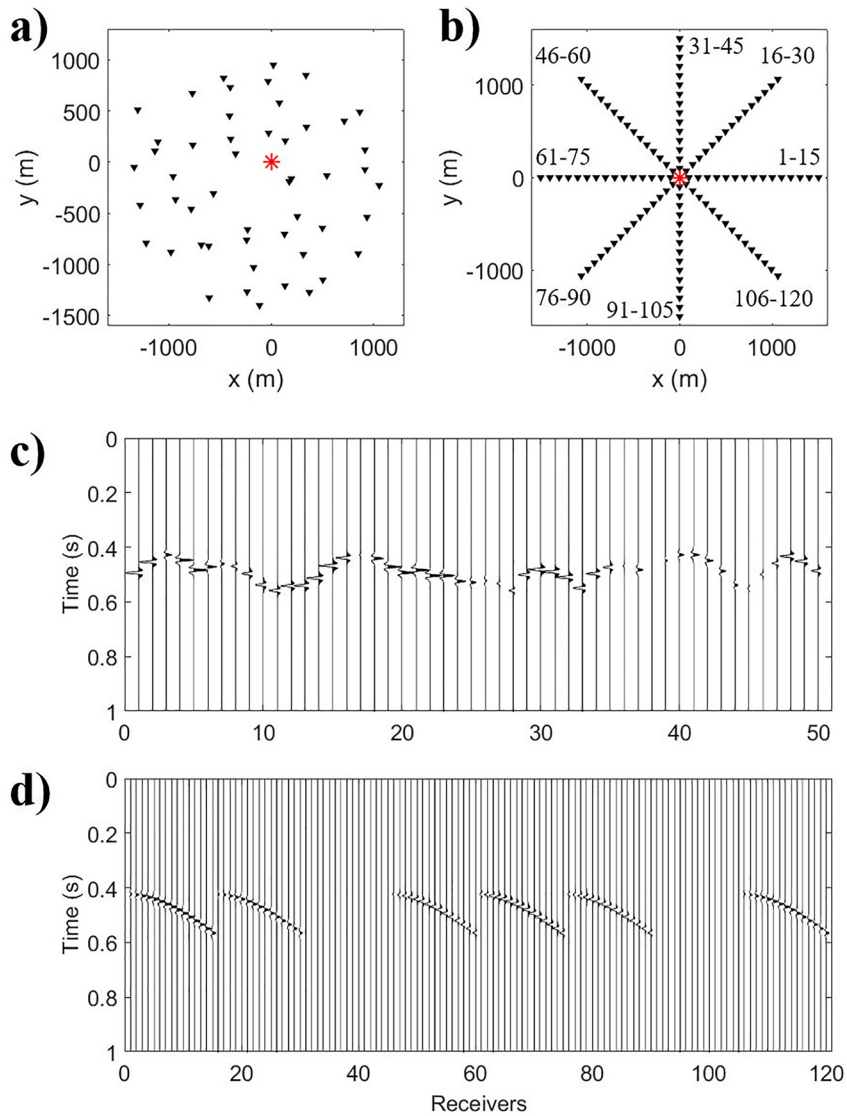

Figure 21. Two test samples with different geometry. (a) Shows the sparse surface array with 50 receivers (black inverted triangles) extracted from field geometry shown in Figure 3; (b) shows the star-like surface array with 120 receivers (black inverted triangles), which are distributed on 8 arms with an interval of 100 m. The numbers at the end of the arms indicate the serial numbers of receivers. The red stars indicate the planar projections of sources. (c) and (d) are synthetic waveforms for the sparse array and the star-like array, respectively.

7. Conclusions

The migration-based location method is necessary to efficiently locate microseismic events with low SNR from the surface array. However, the polarity reversal caused by the source mechanisms may result in incorrect locations. Previous studies have introduced many approaches to solving this problem by correcting the polarity in the data domain or developing better imaging conditions in the imaging domain. In this paper, we develop a location method based on deep learning to detect and locate the event from the stacking image for microseismic events. In this method, we first apply the efficient diffraction stacking to compute a migrated source image where the microseismic source appears a quasi-symmetric pattern in both space and time domain. We then input the diffraction stacking image into a modified 3D U-Net which reshapes the quasi-symmetric pattern to a Gaussian distribution centered at the source location so that we can easily detect the source. We train the 3D U-Net by synthetic datasets, which are composed of noise-free data and

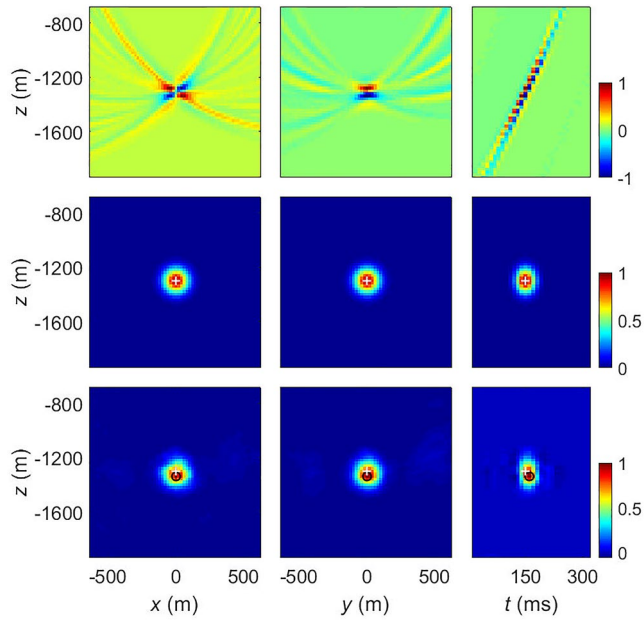

Figure 22. The input, label, and prediction of the sample from the sparse array (Figure 21a). The upper panel shows three slices of diffraction stacking image that is the input data of the network. The middle panel indicates three slices of a Gaussian distribution centered on the source location which is the label of the network. The bottom panel shows three slices of the prediction. The white crosses show the maximum of the label and indicate the true source location. The black circles show the maximum of prediction and indicate the source location predicted by the trained network.

noisy data with an SNR of one. The trained network shows a good performance on the test datasets with an SNR of 1/2. In the application of the field data, our proposed location method can reliably detect and locate microseismic events with low SNR. However, this location procedure can be further improved because of the missing detection for visible events.

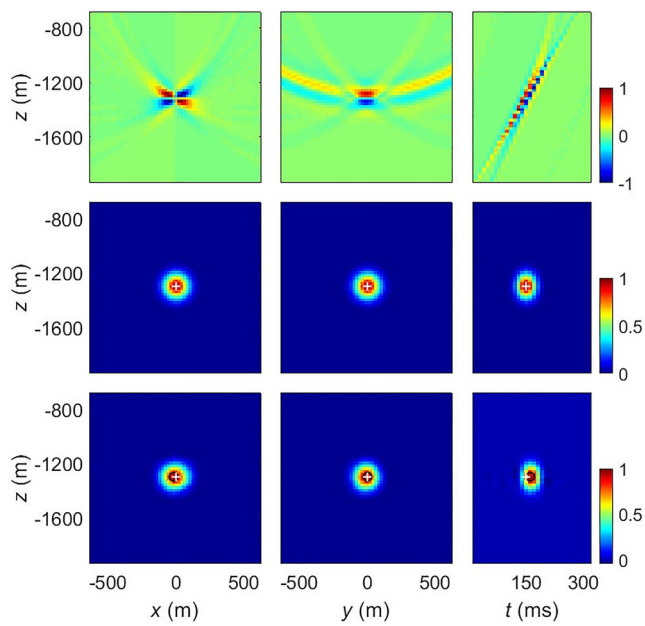

Figure 23. The input, label, and prediction of the sample from the star array (Figure 21b). The upper panel shows three slices of diffraction stacking image that is the input data of the network. The middle panel indicates three slices of a Gaussian distribution centered on the source location that is the label of the network. The bottom panel shows three slices of the prediction. The white crosses show the maximum of the label and indicate the true source location. The black circles show the maximum of prediction and indicate the source location predicted by the trained network.

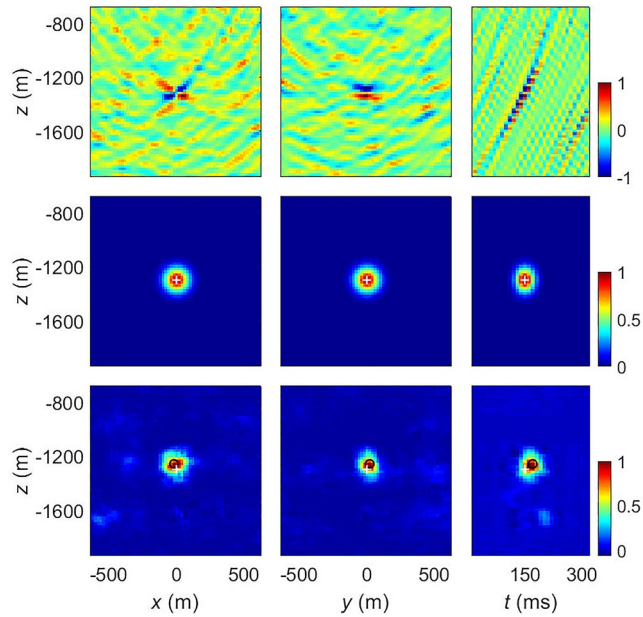

Figure 24. The input, label, and prediction of the noisy sample from the sparse array (Figure 21a). The upper panel shows three slices of diffraction stacking image that is the input data of the network. The middle panel indicates three slices of a Gaussian distribution centered on the source location that is the label of the network. The bottom panel shows three slices of the prediction. The white crosses show the maximum of the label and indicate the true source location. The black circles show the maximum of prediction and indicate the source location predicted by the trained network.

Data Availability Statement

The codes and two case samples are available at https://doi.org/10.5281/zenodo.6075166. The uploaded file contains the network, the trained model, two cases, the script for prediction, and the script for drawing. The whole datasets are huge (about 60 GB) due to each training sample being a 4D matrix obtained by diffraction stacking. Thus, instead of providing the training datasets, we introduce the process of data generation here: (a) designing geometry with an appropriate velocity model; (b) synthesizing a series of waveforms for sources with random location and mechanism, and the forward simulation can refer to Zhang and Chen (2006) and Zhang et al. (2012); (c) diffraction stacking and this step can be simply realized according to Equation 3; (d) reshaping the diffraction stacking image matrix into appropriate size to meet the requirements of network input.

Acknowledgments
This study was supported by the National Natural Science Foundation of China (Grant Nos. 42074056, U1901602), Shenzhen Science and Technology Program (KQTD20170810111725321), and Shenzhen Key Laboratory of Deep Offshore Oil and Gas Exploration Technology (Grant No. ZDSYS20190902093007855). The computation is supported by Center for Computational Science and Engineering of Southern University of Science and Technology.

References

Anikiev, D., Valenta, J., Staněk, F., & Eisner, L. (2014). Joint location and source mechanism inversion of microseismic events: Benchmarking on seismicity induced by hydraulic fracturing. *Geophysical Journal International*, *198*(1), 249–258. https://doi.org/10.1093/gji/ggu126

Artman, B., Podladtchikov, I., & Witten, B. (2010). Source location using time-reverse imaging. *Geophysical Prospecting*, *58*(5), 861–873. https://doi.org/10.1111/j.1365-2478.2010.00911.x

Chambers, K., Dando, B. D. E., Jones, G. A., Velasco, R., & Wilson, S. A. (2014). Moment tensor migration imaging. *Geophysical Prospecting*, *62*(4), 879–896. https://doi.org/10.1111/1365-2478.12108

Duncan, P. M. (2005). Is there a future for passive seismic? In *67th EAGE Conference and Exhibition 2005*. European Association of Geoscientists and Engineers. https://doi.org/10.3997/1365-2397.23.6.26577

Ge, Q., Han, L., & Cai, Z. (2019). Reverse travel time imaging of microseismic location. *Exploration Geophysics*, *50*(3), 281–296. https://doi.org/10.1080/08123985.2019.1605827

Geiger, L. (1912). *Probability Method for the Determination of Earthquake Epicenters from the Arrival Time Only* (Vol. 8, pp. 60–71). Bulletin of Saint Louis University.

Grigoli, F., Cesca, S., Amoroso, O., Emolo, A., Zollo, A., & Dahm, T. (2014). Automated seismic event location by waveform coherence analysis. *Geophysical Journal International*, *196*(3), 1742–1753. https://doi.org/10.1093/gji/ggt477

Grigoli, F., Cesca, S., Vassallo, M., & Dahm, T. (2013). Automated seismic event location by travel-time stacking: An application to mining induced seismicity. *Seismological Research Letters*, *84*(4), 666–677. https://doi.org/10.1785/0220120191

Hung, S.-H., Dahlen, F. A., & Nolet, G. (2001). Wavefront healing: A banana-doughnut perspective. *Geophysical Journal International*, *146*(2), 289–312. https://doi.org/10.1046/j.1365-246x.2001.01466.x

Ito, A. (1985). High-resolution relative hypocenters of similar earthquakes by cross-spectal analysis method. *Journal of Physics of the Earth*, *33*(4), 279–294. https://doi.org/10.4294/jpe1952.33.279

Kao, H., & Shan, S. J. (2004). The source-scanning algorithm: Mapping the distribution of seismic sources in time and space. *Geophysical Journal International*, *157*(2), 589–594. https://doi.org/10.1111/j.1365-246x.2004.02276.x

Kao, H., & Shan, S. J. (2007). Rapid identification of earthquake rupture plane using source-scanning algorithm. *Geophysical Journal International*, *168*(3), 1011–1020. https://doi.org/10.1111/j.1365-246x.2006.03271.x

Kao, H., Shan, S.-J., Dragert, H., Rogers, G., Cassidy, J. F., Wang, K., et al. (2006). Spatial-temporal patterns of seismic tremors in northern Cascadia. *Journal of Geophysical Research*, *111*, B03309. https://doi.org/10.1029/2005jb003727

Kawakatsu, H., & Montagner, J. P. (2008). Time-reversal seismic-source imaging and moment-tensor inversion. *Geophysical Journal International*, *175*(2), 686–688. https://doi.org/10.1111/j.1365-246x.2008.03926.x

Kriegerowski, M., Petersen, G. M., Vasyura-Bathke, H., & Ohrnberger, M. (2019). A deep convolutional neural network for localization of clustered earthquakes based on multistation full waveforms. *Seismological Research Letters*, *90*(2A), 510–516. https://doi.org/10.1785/0220180320

Langet, N., Maggi, A., Michelini, A., & Brenguier, F. (2014). Continuous kurtosis-based migration for seismic event detection and location, with application to Piton de la Fournaise Volcano, La Réunion. *Bulletin of the Seismological Society of America*, *104*(1), 229–246. https://doi.org/10.1785/0120130107

Li, J., Kuleli, H. S., Zhang, H., & Toksöz, M. N. (2011). Focal mechanism determination of induced microearthquakes in an oil field using full waveforms from shallow and deep seismic networks. *Geophysics*, *76*(6), 87. https://doi.org/10.1190/geo2011-0030.1

Li, J., Wu, X., & Hu, Z. (2021). Deep learning for simultaneous seismic image super-resolution and denoising, (Vol. 60, pp. 1–11). *IEEE Transactions on Geoscience and Remote Sensing*. https://doi.org/10.1109/TGRS.2021.3057857

Li, Z., Sheng, G., Wang, W., Cui, Q., & Zhou, D. (2014). The multi-component microseismic time reverse interferometric location based on joint observation of surface and borehole. *Oil Geophysical Prospecting*, *49*(4), 661–671.

Li, Z., & Zhao, B. (2012). Microseism monitoring system for coal and gas outburst. *International Journal of Computer Science Issues*, *9*(5), 24–28. Retrieved from http://www.ijcsi.org/articles/Microseism-monitoring-system-for-coal-and-gas-outburst.php

Liang, C., Yu, Y., Yang, Y., Kang, L., Yin, C., & Wu, F. (2016). Joint inversion of source location and focal mechanism of microseismicity. *Geophysics*, *81*(2), KS183–KS191. https://doi.org/10.1190/geo2015-0272.1

Lyu, B., & Nakata, N. (2020). Iterative passive-source location estimation and velocity inversion using geometric-mean reverse-time migration and full-waveform inversion. *Geophysical Journal International*, *233*(3), 1935–1947. https://doi.org/10.1093/gji/ggaa428

Maxwell, S. C. (2014). *Microseismic imaging of hydraulic fracturing: Improved engineering of unconventional shale reservoirs*. Society of Exploration Geophysicists.

Maxwell, S. C., & Urbancic, T. I. (2001). The role of passive microseismic monitoring in the instrumented oil field. The *Leading Edge*, *20*(6), 636–639. https://doi.org/10.1190/1.1439012

Nakata, N., & Beroza, G. C. (2015). Reverse-time migration for microseismic sources using the geometric mean as an imaging condition. *Geophysics*, *81*(2), KS51–KS60. https://doi.org/10.1190/segam2015-5851848.1

Oren, C., & Shragge, J. (2019). 3D anisotropic elastic time-reverse imaging of surface-recorded microseismic data. *Technical Program Expanded Abstracts*, SEG. https://doi.org/10.1190/segam2019-3215476.1

Peng, Z., & Zhao, P. (2009). Migration of early aftershocks following the 2004 Parkfield earthquake. *Nature Geoscience*, *2*, 877–881. https://doi.org/10.1038/ngeo697

Perol, T., Gharbi, M., & Denolle, M. (2018). Convolutional neural network for earthquake detection and location. *Science Advances*, *4*(2), e1700578. https://doi.org/10.1126/sciadv.1700578

Richards, P. G., Waldhauser, F., Schaff, D., & Kim, W. Y. (2006). The applicability of modern methods of earthquake location. *Pure and Applied Geophysics*, *163*(2–3), 351–372. https://doi.org/10.1007/s00024-005-0019-5

Rocha, D., Sava, P., Shragge, J., & Witten, B. (2019). 3D passive wavefield imaging using the energy norm. *Geophysics*, *84*(2), KS13–KS27. https://doi.org/10.1190/GEO2018-0251.1

Ronneberger, O., Fischer, P., & Brox, T. (2015). U-net: Convolutional networks for biomedical image segmentation. In *International Conference on Medical image computing and computer-assisted intervention* (pp. 234–241). Springer. https://doi.org/10.1007/978-3-319-24574-4_28

Saad, O. M., & Chen, Y. (2020). Automatic waveform-based source-location imaging using deep learning extracted microseismic signals. *Geophysics*, *85*(6), KS171–KS183. https://doi.org/10.1190/geo2020-0288.1

Shelly, D., Beroza, G. C., & Ide, S. (2007). Non-volcanic tremor and low-frequency earthquake swarms. *Nature*, *446*, 305–307. https://doi.org/10.1038/nature05666

Shi, P., Doug, A., Sebastian, R., Andy, N., & Yuan, S. (2018). Automated seismic waveform location using multichannel coherency migration (MCM)–I. theory. *Geophysical Journal International*, *216*(3), 1842–1866. https://doi.org/10.1093/gji/ggy132

Tian, X., Zhang, W., Zhang, X., Zhang, J., Zhang, Q., Wang, X., & Guo, Q. (2020). Comparison of single-trace and multiple-trace polarity determination for surface microseismic data using deep learning. *Seismological Research Letters*, *91*(3), 1794–1803. https://doi.org/10.1785/0220190353

Trojanowski, J., & Eisner, L. (2017). Comparison of migration-based location and detection methods for microseismic events. *Geophysical Prospecting*, *65*(1), 47–63. https://doi.org/10.1111/1365-2478.12366

Waldhauser, F., & Ellsworth, W. L. (2000). A double-difference earthquake location algorithm: Method and application to the northern hayward fault, California. *Bulletin of the Seismological Society of America*, *90*(6), 1353–1368. https://doi.org/10.1785/0120000006

Wang, C. L., Cheng, J. B., Yin, C., & Liu, H. (2013). Microseismic events location of surface and borehole observation with reverse-time focusing using interferometry technique. *Chinese Journal of Geophysics*, *56*(9), 3184–3196. https://doi.org/10.6038/cjg20130931

Wu, X., Geng, Z., Shi, Y., Pham, N., Fomel, S., & Caumon, G. (2020). Building realistic structure models to train convolutional neural networks for seismic structural interpretation. *Geophysics*, *85*(4), WA27–WA39. https://doi.org/10.1190/geo2019-0375.1

Xu, J., Zhang, W., Chen, X., & Guo, Q. (2020). An effective polarity correction method for microseismic migration-based location. *Geophysics*, *85*(4), KS115–KS125. https://doi.org/10.1190/geo2019-0497.1

Yan, S., & Wu, X. (2021). Seismic horizon extraction with dynamic programming. *Geophysics*, *86*(2), IM51–IM62. https://doi.org/10.1190/geo2020-0039.1

Yilmaz, O. (2001). *Seismic data analysis, Processing, Inversion and Interpretation of Seismic Data*, (Vol. 1, pp. 485–486). Society of Exploration Geophysicists. https://doi.org/10.1190/1.9781560801580

Zhang, Q., & Zhang, W. (2022). An efficient diffraction stacking interferometric imaging location method for microseismic events. *Geophysics*, *87*(3), 1–45. https://doi.org/10.1093/gji/ggab504

Zhang, W., & Chen, X. (2006). Traction image method for irregular free surface boundaries in finite difference seismic wave simulation. *Geophysical Journal International*, *167*(1), 337–353. https://doi.org/10.1111/j.1365-246x.2006.03113.x

Zhang, W., Zhang, Z., & Chen, X. (2012). Three-dimensional elastic wave numerical modelling in the presence of surface topography by a collocated-grid finite-difference method on curvilinear grids. *Geophysical Journal International*, *190*(1), 358–378. https://doi.org/10.1111/j.1365-246x.2012.05472.x

Zhang, X., & Zhang, J. (2016). Microseismic search engine for real-time estimation of source location and focal mechanism. *Geophysics*, *81*(5), KS169–KS182. https://doi.org/10.1190/geo2015-0695.1

Zhang, X., Zhang, J., Yuan, C., Liu, S., Li, W., & Li, W. (2020). Locating induced earthquakes with a network of seismic stations in Oklahoma via a deep learning method. *Scientific Reports*, *10*(1), 1941. https://doi.org/10.1038/s41598-020-58908-5

Zhebel, O., & Eisner, L. (2015). Simultaneous microseismic event localization and source mechanism determination. *Geophysics*, *80*(1), KS1–KS9. https://doi.org/10.1190/geo2014-0055.1

Zhou, Y., Zhang, Q., & Zhang, W. (2022). PS interferometric imaging condition for microseismic source elastic time-reversal imaging. *Geophysical Journal International*, *229*(1), 505–521. https://doi.org/10.1190/geo2021-0233.1

Zhou, Y., & Zhang, W. (2017). PS interferometric correlation imaging condition for seismic source elastic time-reversal imaging, *Microseismic Technologies and Applications* (pp. 86–89). SEG, Workshop. https://doi.org/10.1190/Microseismic2017-022